The impact of ZnO nanotube on the performance of hybrid inorganic/organic light-emitting diode as a single-mode ring-core UV waveguide

Rezaie, Mahdiyar Nouri; Mohammadnejad, Shahram & AHADZADEH, Shabnam
(2022) The impact of ZnO nanotube on the performance of hybrid inorganic/organic light-emitting diode as a single-mode ring-core UV waveguide. In: Surfaces and Interfaces, 28 (Art N° 101666).

DOI: 10.1016/j.surfin.2021.101666
Handle: http://hdl.handle.net/1942/37151

The impact of ZnO nanotube on the performance of hybrid inorganic/organic light-emitting diode as a single-mode ring-core UV waveguide

Mahdiyar Nouri Rezaie [a], Shahram Mohammadnejad [a]*, Shabnam Ahadzadeh [b]

[a] Department of Electrical Engineering, Iran University of Science and Technology, Narmak, Tehran, Iran

[b] Hasselt University, Institute for Materials Research (IMO-IMOMEC), Wetenschapspark 1, Diepenbeek B-3590, Belgium

*Corresponding author Tel: +98 21 73225630, Fax: +98 21 73225777

P.O. Box: 1684613114, Narmak, Tehran, Iran

E-mail address: Shahramm@iust.ac.ir

Abstract

After a systematic survey in hybrid inorganic/organic light-emitting heterostructure devices based on ZnO in the last decay, in this novel work, the impact of the single-mode ring-core waveguide based on ZnO nanotube (NT)/MEH-PPV for ultraviolet organic light-emitting diode (UV-OLED) application has been carefully scrutinized for the first time. The proposed structure has been fabricated, simulated and compared with conventional ZnO nanorod (NR)/MEH-PPV structure. To synthesize ZnO NTs, the as-grown chemical bath deposited ZnO NRs have been etched in KCL solution in various molar (M) concentration, etching time and etching temperature. The optimized etching condition is obtained in 1 M concentration of KCL solution, 4 h etching time and 90 ℃ temperature. The structural properties (such as strain, stress and texture coefficient), electrical properties (such as band gap energy) and optical properties (such as Urbach energy, absorbance and photoluminescence spectra) of ZnO NTs have been investigated, systematically. In continue, hybrid UV-OLEDs have been fabricated based on ZnO NRs and ZnO NTs. According to the results, ZnO NT-based OLED depicts superior electrical and optical results including lower turn-on voltage (11.2 V < 15 V) and higher UV peak in electroluminescence spectra with respect to ZnO NR-based device. To acquire more enlightenment about UV emission mechanism, the proposed devices have been simulated through Silvaco TCAD and Lumerical FDTD software. The results from simulations illustrate great agreement with experimental results. Higher radiative recombination rate, higher Purcell factor and single-mode waveguiding effect of ring-core ZnO NT lead to major superiority of the ZnO NT-based UV-OLED fabricated and simulated in this work.

Keywords:

ZnO nanotube, Hybrid light-emitting diode, ring-core waveguide, single-mode waveguide

1. Introduction

Nowadays, novel optoelectronic devices based on polymers and nanostructures are well capable of providing the market demand. Although organic light-emitting diodes (OLEDs) are widely utilized and scrutinized in recent years, achieving an optimized, stable and high-efficient product is debatable until now. One of the most desired approaches to increase the efficiency and light outcoupling of the OLEDs is utilizing waveguides (such as ring-core waveguides) within the light-emitting devices [1-5]. Moreover, there are variety of applicable organic and inorganic materials to provide hybrid optoelectronic devices. Among them, zinc oxide (ZnO) and poly [2-methoxy-5-(2-ethylhexyloxy)-1,4-phenylenevinylene] (MEH-PPV) have been considered as proper materials for light-emitting diodes based on inorganic/organic (I/O) hybrid heterojunctions [6, 7]. ZnO is known as an environmental-friendly material with some advantages including direct bandgap of 3.37 eV [8], large Wannier-Mott exciton binding energy of 60 meV [9], easy growth of various nanostructures [10] and high electrical conductivity [11]. Moreover, MEH-PPV is introduced as a conjugated polymer with uncomplicated production process and low cost [12]. According to high band alignment and low lattice mismatch of ZnO and MEH-PPV, their combination and growth process are acceptable [13]. From our previous review study related to ZnO based heterojunction OLEDs [6], many scholars have been investigated and designed LEDs based on these two materials. For instance, Zhao et al. offered the structure based on ZnO nanorod (NR)/MEH-PPV that ZnO NRs are grown by hydrothermal method [14]. The growth methods of ZnO nanostructures can be divided into two categories as solution-based chemical techniques [15-18] and physical methods [19]. To grow the ZnO nanostructure with solution-based chemical approaches, choosing a proper seed layer is essential. Aluminum-doped ZnO (AZO) plays a significant role as a seed layer among different materials which could be a superior choice due to the high physical characteristics [20, 21]. In the continuation of this issue, Rezaie et al. fabricated OLED devices based on indium tin oxide (ITO)/AZO/ZnO NR/MEH-PPV/Al and ITO/ZnO/ZnO

NR/MEH-PPV/Al layers which the first one is demonstrated superior capabilities including higher average transmittance, higher surface morphology, lower trap concentrations and better optical characteristics compared to the second structure [22]. As discussed above, ZnO NRs are mostly utilized to fabricate hybrid LEDs, but there is no trace of any cooperation of ZnO nanotubes (NTs) in OLEDs [6]. ZnO NTs can be achieved by the dissolution of the NRs, which is accessible by applying KCl chemical solution [23]. Although both NRs and NTs are favorable for LED preparation, NTs due to their higher surface to bulk aspect ratio [6, 24], tunable band gap energy [25] and higher porosity [26, 27] are more advantageous to OLED applications. Since the ZnO NT shape is annular, it can fill with organic polymers. If the refractive index of the filled polymer becomes lower than ZnO NT, ZnO NT acts as ring-core waveguide. The produced UV light in ZnO NT can propagate through the walls of NTs since the wall is surrounded with MEH-PPV cladding with lower refractive index. If the numerical aperture of the waveguide which relates to the refractive index of the ZnO NT core and MEH-PPV cladding, width of the ZnO NT's wall and the wavelength of the propagated UV light satisfy the conditions, the guided wave becomes single-mode, coherent, co-phase and uniform which leads to higher external quantum efficiency of OLED.

After a systematic survey in hybrid I/O light-emitting heterostructure devices based on ZnO in the last decay [6], in this novel work, the impact of the single-mode ring-core waveguide based on ZnO NT/MEH-PPV heterostructure for UV-OLED application has been carefully scrutinized for the first time. The proposed structure has been fabricated and simulated through Silvaco TCAD and FDTD Lumerical software and compared with conventional ZnO NR/MEH-PPV structure. The morphological and physical properties including X-ray diffraction (XRD) pattern, field emission scanning electron microscopy (FE-SEM), selected-area electronic diffraction pattern (SAED) and transmission electron microscopy (TEM) images have been done for ZnO NT samples with various etching conditions. In continue, two OLEDs with the structure of

ITO/AZO/ZnO NR array/MEH-PPV/Al (device A) and ITO/AZO/ZnO NT array/MEH-PPV/Al (device B) have been fabricated and compared. The structural, electrical and optical features involving current density versus voltage curve, strain, stress, texture coefficient, Urbach energy, band gap energy, trap concentration, characteristic energy, absorbance spectra, photoluminescence (PL) and electroluminescence (EL) spectra of ZnO NT samples and devices have been studied and compared. Moreover, the wave guiding effect for both ZnO NR and NTs, the opto-electronic mechanism of the UV light generation and guiding as well as their role on enhancing the EL intensity has been studied and investigated in this paper. Ultimately, radiative recombination rate, electric field distribution in waveguides and Purcell factor of the structures have been simulated and analyzed.

2. Experimental details

2.1. Synthesis of ZnO NRs arrays on ITO/AZO substrate

To synthesize ZnO NRs, 100 nm-thick-ITO layer is deposited with radio frequency (RF) magnetron sputtering on glass substrate for 10 min at the vacuum pressure of 5×10^{-6} Torr. Besides, by applying the sputtering apparatus at frequency of 13.56 MHz and power of 175 W, a layer of AZO with the thickness of 100 nm was sputtered on ITO substrate to guarantee the vertical and uniform growth of ZnO NTs. Wet chemical bath deposition (CBD) method with the growth temperature of 90°C was considered to synthesize the ZnO NRs with 12 mM hexamethylenetetramine ($(CH_2)_6N_4$, Merck) (HMTA) and 24 mM zinc nitrate hexahydrate ($Zn(NO_3)_2.6H_2O$, Merck) in deionized (DI) water solution. The molar (M) proportion of HMTA:$Zn(NO_3)_2$-$6H_2O$ is 0.5:1 [28, 29]. To remove all residual organics, the ZnO NRs with the height of 1500 nm and ITO/AZO layer with the thickness of 200 nm were annealed at 400 °C for 30 min.

According to the survival of the fastest model defined by Van der Drift, self-assembly mechanism leads to growth of ZnO NR arrays [30]. The survival of the fastest model poses that the nucleation sites which have rapid growth directions are preserved, while other directions are ceased due to crossing higher NRs. Moreover, growth velocities of: $v_{(0001)} > v_{(01\overline{1}1)} > v_{(01\overline{1}0)} > v_{(000\overline{1})}$ show different crystal growth rate of ZnO NR planes [31]. As a result, since growth velocity of (0001) dominates in ZnO NRs, synthesis of arrays occurs along the c-axis [22]. Besides, the heterogeneous nucleation sites on AZO layers cause growth of well-aligned NRs that stems from several advantageous including high energetic reaction, low barrier of nucleation energy, easy creation of nucleation and negligible lattice mismatch between nanostructures and the substrate/seed layer [32, 33]. There are some of the chemical reactions employed in the process of synthesis of ZnO NR arrays which are listed as Eqs. (1) to (8) [29, 34-36]:

$$Zn(NO_3)_2 + C_6H_{12}N_4 \rightarrow [Zn(C_6H_{12}N_4)]^{2+} + 2NO_3^- \quad (1)$$

$$C_6H_{12}N_4 + 6H_2O \leftrightarrow 4NH_3 + 6CH_2O \quad (2)$$

$$NH_3 + H_2O \leftrightarrow NH_4^+ + OH^- \quad (3)$$

$$Zn^{2+} + 4OH^- \rightarrow [Zn(OH)_4]^{2-} \quad (4)$$

$$Zn^{2+} + 4NH_3 \leftrightarrow [Zn(NH_3)_4]^{2+} \quad (5)$$

$$Zn^{2+} + 2OH^- \leftrightarrow Zn(OH)_2 \leftrightarrow ZnO + H_2O \quad (6)$$

$$Zn^{2+} + C_6H_{12}N_4 \rightarrow [Zn(C_6H_{12}N_4)]^{2+} \quad (7)$$

$$[Zn(C_6H_{12}N_4)]^{2+} + 2OH^- \rightarrow ZnO + H_2O + C_6H_{12}N_4 \quad (8)$$

From Eqs. (2) and (3), HMTA plays main role to provide and control the concentration of the hydroxyl ion (OH^-) and pH buffer (NH_4^+) and enhances the growth of ZnO NRs along the (0001) plane. Eq. (6) illustrates the beginning of the NRs growth which arises from creation of nucleation

sites after catching the OH^- anions by the Zn^{2+} cations. Because of the hexagonal shapes of ZnO NRs, more ions are absorbed by Zn-terminated top polar planes, while O-terminated bottom polar planes stay inactive [37]. Furthermore, spatial resonance phenomenon that comes from $Zn[(OH)_4]^{2-}$ ions is another crucial effect which involves in the faster rate of perpendicular synthesis of ZnO NRs [37]. The anisotropic growth leads to faster rate of [0001] plane rather than others [32]. After growing ZnO NRs, ZnO NTs' formation was achieved by etching the NRs under various parameters including etching times, KCl solution concentrations and etching temperatures.

2.2. Synthesis of ZnO nanotube arrays on ITO/AZO substrate

In the following, the ZnO NRs were carved by placing up toward down in a potassium chloride aqueous solution (KCl) which related reactions are shown by Eq. (9) and Eq. (10) [38, 39]:

$$KCl + H_2O \rightarrow KOH^- + HCl \quad (9)$$

$$ZnO + 2OH^- \rightarrow {ZnO_2}^{2-} + H_2 \quad (10)$$

Furthermore, a favorable etching and conversion from NR into NT have been happened since there is no trace of any kind of assistant reagents. In this work, the temperature, time of NRs etching and concentration of KCl solution are variable and modified to optimize the process. To achieve proper NTs, the mentioned variables were optimized.

2.3. Making hybrid OLEDs

Ultimately, I/O near ultraviolet LEDs were fabricated by growing the ZnO nanostructures on ITO/AZO substrate and spin-coating of 5 mg/ml of MEH-PPV solution (dissolved in toluene) on them at 3000 rpm for 8 times [22]. The thickness of MEH-PPV layer is considered to be 1600 nm which is higher than ZnO nanostructures height and act as a barrier against the current leakage into the electrode. In the last step, to achieve100 nm-thick-cathode layer, the evaporation technique was employed to deposit the aluminum (Al) layer on MEH-PPV [22].

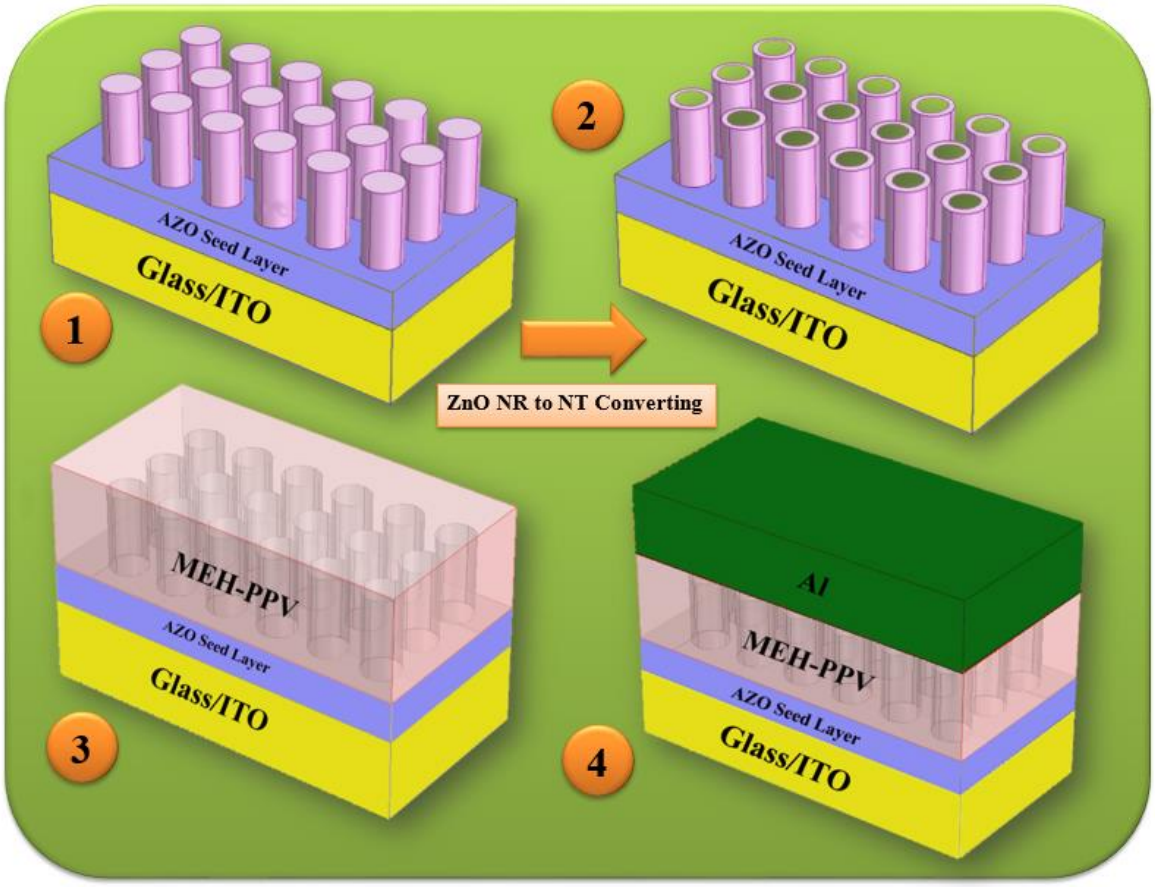

Fig. 1. Schematic diagram of the UV-OLED fabrication; (1) Synthesizing of ZnO NR on AZO seed layer via CBD method, (2) Converting ZnO NR into NT by wet etching process in various KCl solution concentration, etching time and temperature, (3) Spin-coating of MEH-PPV on ZnO NT structure, (4) Evaporating Al electrode on the top of the device.

2.4. Structural, electrical and optical measurements

The structural and physical features of ZnO nanostructures were observed by various techniques including Hitachi S-4160 at the voltage of 20 KV, FE-SEM images, JEM-2010-JEOL-Japan TEM and Philips Expert pro XRD analysis using (λ = 1.5418 Å) with angel step size of 0.02°. Furthermore, Source Measurement Unit (SMU), Cary Eclipse fluorescence spectrophotometer at the wavelength of 325 nm with He-Cd laser as the source of excitation and a compact spectrometer (Thorlabs Inc, CCS100, 350 – 700 nm) connected to computer were used to study the electrical and optical characteristics of fabricated I/O LEDs, including current density-voltage (J-V) curves,

PL and EL spectra of devices, respectively. The schematic diagram of the UV-OLED fabrication is illustrated in Fig. 1.

3. Results and discussion

3.1. Physical characteristics of ZnO NT arrays

As mentioned before, the ZnO NTs are perpendicularly grown on AZO seed layer. To investigate the physical and structural characteristics of ZnO NTs, FE-SEM images and XRD analysis considering etching time, KCl solution concentration and temperature are shown in Figs. 2, 3 and 4. FE-SEM images of ZnO NTs under the condition of 1 M KCl concentration solution at 90 °C for variable etching time of 0, 2, 4 and 6 hours (h) are represented in Figs. 2a, 2b, 2c and 2d, respectively. ZnO NRs are uniformly grown in a large area which create a proper sample for converting ZnO NRs to NTs. From Fig. 2d, it is obvious that after 6 h, all of the planes (including polar and non-polar) have been etched which leads to formation of uneven top surfaces. Besides, Fig. 2c demonstrates that after 4 h of etching, the intensity of non-polar planes decreases at a slow rate, while the reduction in the non-polar planes intensity is more considerable when time passes 6 h which is not desired. Fig. 2e illustrates the XRD pattern of the of synthesized ZnO NTs under the etching condition of 1 M concentration of KCl, 90 ˚C temperature and various etching times of 0 (ZnO NR), 2, 4 and 6 h. For all samples (during each process) the most intense peak has been occurred at (002) plane which demonstrates a perfectly aligned perpendicular orientation of ZnO NTs grown on ITO/AZO substrates. According to Fig. 2e, by increasing the etching time from 0 to 6 h, the intensity of peaks related to (102) and (101) planes reduce under a constant temperature of 90 °C and 1 M concentration of KCl solution.

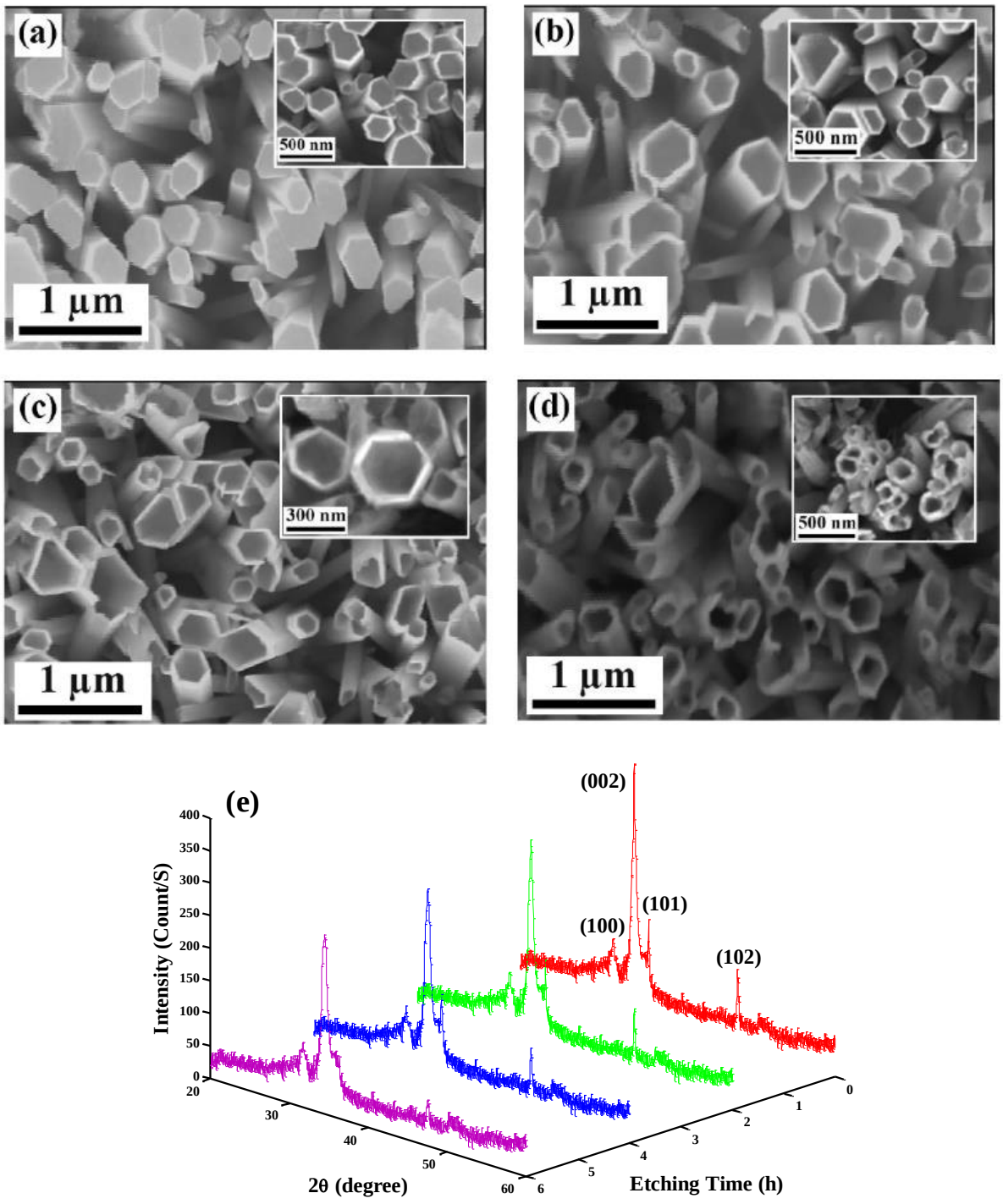

Fig. 2. FE-SEM images of synthesized ZnO NTs under the etching condition of 1 M concentration of KCl, 90 ˚C temperature and various etching times of (a) 0 h (ZnO NR), (b) 2 h, (c) 4 h and (d) 6 h; (e) XRD of ZnO NTs carved in various etching times.

FE-SEM images for different amount of KCl solution of 1, 2, 3 and 4 M under fixed temperature and etching time of 90 ºC and 4 h are demonstrated in Figs. 3a, 3b, 3c and 3d, respectively. Since

most high surface energies have occurred on defect-full areas of NRs, even at 1 M concentration of KCl solution, the process of rod to tube conversion is possible (shown in Fig. 3a). Although the FE-SEM images related to NTs in the solution of 2 and 3 M are roughly similar, only small area of ZnO NT related to 4 M etching solution is remained and most areas of the ZnO NRs are washed, (see Fig. 3d). In accordance with Fig. 3e, under fixed temperature and etching time, by increasing the amount of KCl solution from 1 up to 4 M, the peak intensity of (102) and (101) non-polar planes have decreased from 95 to 63 and 152 downward to 95, respectively. The reduction in non-polar peak intensity originates from the etching of the NRs and decrement of (002) dominant peaks which reduces the height of the ZnO NTs. Besides, Fig. 3e shows that the intensity of (100) peak for 4 M concentration of KCL solution increased which results in some flips on the ZnO NTs.

FE-SEM images of NTs grown at temperatures of 80, 85, 90 and 95 ˚C at 1 M concentration of KCl solution for 4 h are depicted in Figs. 4a, 4b, 4c and 4d, respectively. A perfect vision of ZnO NTs both in the inner and outer walls can be seen. Moreover, Fig. 4e depicts XRD pattern of ZnO NTs under condition of 4 h etching time and 1 M concentration of KCL solution that the temperature varies between 80, 85, 90 and 95 ˚C. It is obvious that by increasing the growth temperature, a reduction in the intensity of (002) polar plane appears. In contrast with XRD patterns related to changeable KCl concentration along with the increase in temperature, the intensity of (102) and (101) peaks increase (for more detail see Table 1). As a result, the shrinkage of NTs length has not occurred until 95 ˚C. Subsequently, the temperature of 90 ˚C can be selected as optimized temperature. At least, according to XRD patterns, the optimized NTs are obtained under the condition of 90 ˚C, 1 M concentration of KCl solution and 4 h carving time.

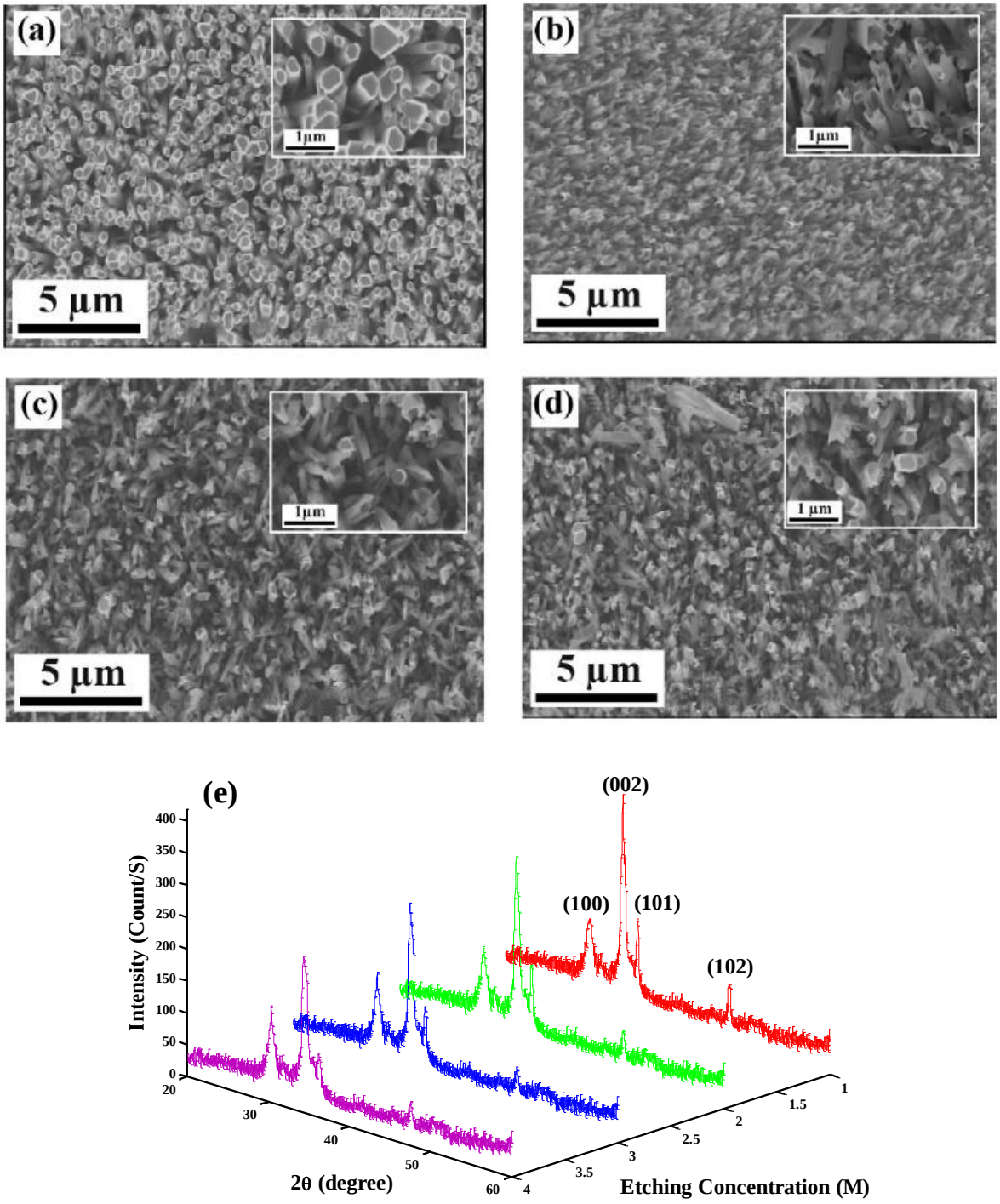

Fig. 3. FE-SEM images of synthesized ZnO NTs under the etching condition of 90 ˚C temperature, 4 h etching time and various KCl concentration of (a) 1 M, (b) 2 M, (c) 3 M and (d) 4 M; (e) XRD of ZnO NTs carved in various etching concentrations.

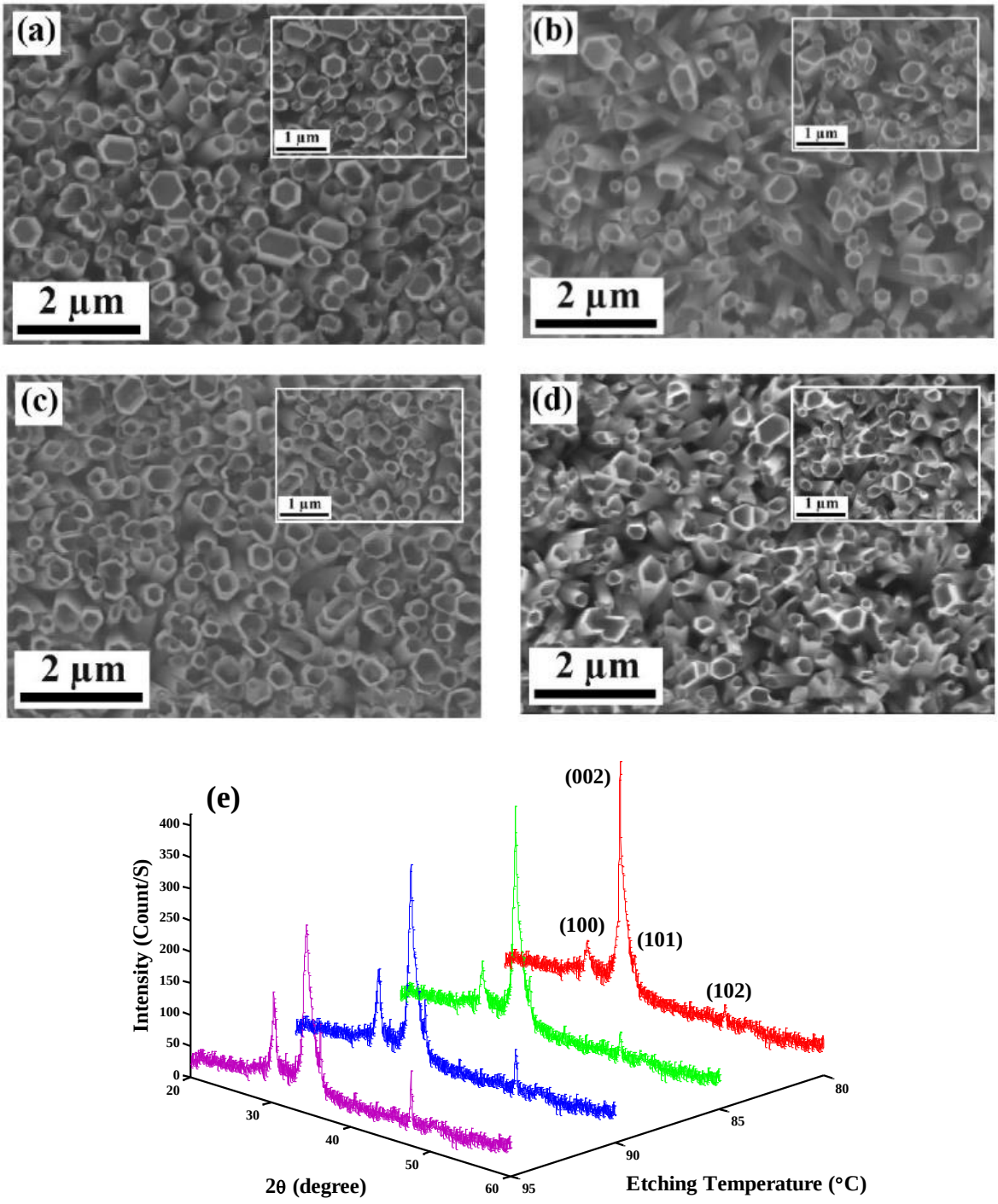

Fig. 4. FE-SEM images of synthesized ZnO NTs under the etching condition of 1 M concentration of KCl, 4 h etching time and various etching temperatures of (a) 80 ˚C, (b) 85 ˚C, (c) 90 ˚C and (d) 95 ˚C; (e) XRD of ZnO NTs carved in various etching temperatures.

In order to see morphological patterns of ZnO nanostructures, cross-sectional FE-SEM and TEM images are depicted in Figs. 5a and 5b, respectively. FE-SEM cross section image before

filling with MEH-PPV is depicted in Fig. 5a and the inset shows FE-SEM cross section image after filling with MEH-PPV. A rod-like morphology of ZnO NRs apparently can be seen in Fig. 5b. In addition, a hexagonal wurtzite crystal for ZnO NT is represented by SAED pattern in the inset of Fig. 5b. A hollow ZnO NT is shown in Fig. 5b. Although the differences between NR and NT samples in this figure is not almost clear, a considerable color difference between the edge and the center of the NT's end expresses unfilled shape of NT [40]. As the center part of the tube is vacant, it has brighter color. Moreover, the inset of Fig. 5b presents a hexagonal wurtzite single-crystal of ZnO NT.

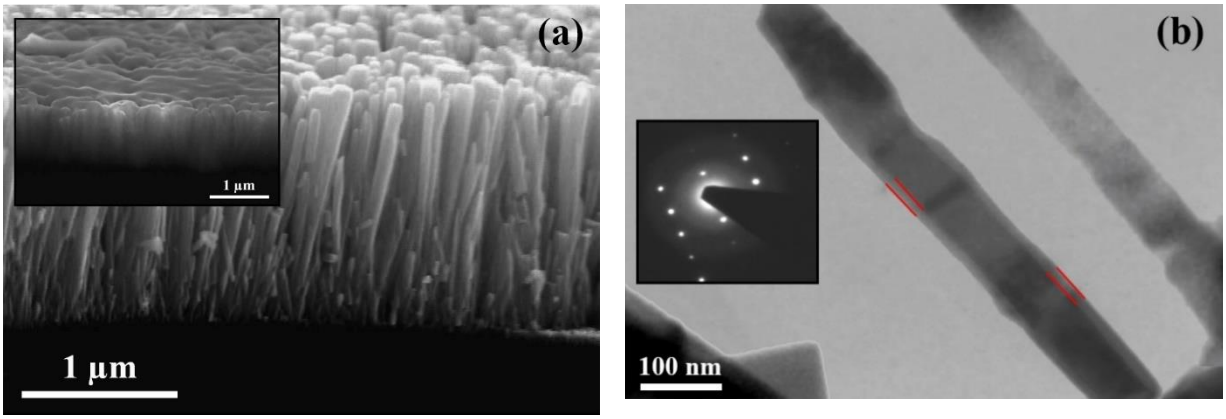

Fig. 5. (a) FE-SEM cross section image before filling with MEH-PPV (The inset shows FE-SEM cross section image after filling with MEH-PPV); (b) TEM image of the ZnO NT (The inset depicts the selected-area electronic diffraction pattern (SAED) of the ZnO NTs).

The other important morphological features of ZnO NTs can be derived from calculation of their strain and stress values. To find the strain value of NTs, Eq. (11) has been applied [8]:

$$\varepsilon = [(c - c_0)/c_0] \times 100\% \qquad (11)$$

where c_0 demonstrates standard lattice parameter of ZnO and c shows the NTs lattice parameters related to each XRD pattern which is extracted by the equation of: $1/d^2 = (h^2 + k^2 + l^2)/c^2$ (where d is interplanar spacing and hkl are the Miller indices) [41, 42]. On the other

side, the stress value of NTs is deduced from Eq. (12) [41] that the value of c_{ij} is defined in Ref. [8, 41]:

$$\sigma = \{[2c_{13}^2 - c_{33}(c_{11} + c_{12})]/(2c_{13})\}.\varepsilon \qquad (12)$$

The strain and stress values of obtained specimens are summarized in Table 1. The positive values of strain for all specimens explains that the unit cell has been stretched along the c-axis [8]. Generally, the etching process causes corrosion in (002) peak by changing time of etching, temperature, and KCL concentration. Therefore, the mentioned reduction in (002) peak is moderately desirable, however, by corrosion in (002) peak, the value of stress and strain increase. Hence, it is critical to make a trade off by adjusting the corrosion rate for (002) peak and other non-polar peaks including (101) and (102).

Table 1. Morphological parameters for ZnO NRs and ZnO NTs (texture coefficient, stress and strain)

	Etching Time (h)				Etching Concentration (M)				Etching Temperature (˚C)			
	0	2	4	6	1	2	3	4	80	85	90	95
$2\theta_{(002)}$ (°) (Standard = 34.4°)	34.30	34.26	34.22	34.02	34.16	33.86	33.64	33.42	34.32	34.28	34.24	34.12
$d_{(002)}$ (Å) (Standard = 2.604 Å)	2.611	2.614	2.617	2.632	2.621	2.644	2.660	2.678	2.609	2.612	2.615	2.624
Strain (ε) (%)	0.268	0.384	0.499	1.075	0.652	1.536	2.150	2.841	0.192	0.307	0.422	0.768
Stress (σ) (GPa)	-0.62	-0.89	-1.16	-2.50	-1.51	-3.57	-5.00	-6.61	-0.44	-0.71	-0.98	-1.78
$TC_{(100)}$	0.028	0.035	0.047	0.057	0.040	0.068	0.090	0.105	0.025	0.035	0.050	0.075
$TC_{(002)}$	3.870	3.846	3.805	3.857	3.856	3.801	3.772	3.749	3.914	3.882	3.841	3.760
$TC_{(101)}$	0.022	0.027	0.035	0.025	0.027	0.037	0.041	0.037	0.014	0.020	0.026	0.036
$TC_{(102)}$	0.077	0.090	0.111	0.059	0.075	0.092	0.095	0.107	0.045	0.061	0.082	0.126

According to Table 1, by increasing the temperature from 80 to 90 ˚C, the stress and strain values slightly increases. However, with the enlargement in temperature from 90 to 95 ˚C, the upward trend in strain and stress has been very strong, which is also evident in the XRD and SEM patterns. Furthermore, for the etching time of zero (ZnO NR), the stress and strain depict the minimum value. However, after 4 h of etching, the stress and strain experience a sharp increment and the walls of the NTs become corroded. Similar to above discussed variables, elevating the etching rate by employing higher value of KCL concentration causes an increment in stress and

strain values. Hence, the KCL concentration above 1 M is unacceptable and optimized values are occurred in the etching temperature of 90 ˚C, 1 M solution concentration of KCl and etching time of 4 h, which have good agreement with our pervious description. The strain and stress in specimens originate from the lattice mismatch between NTs and the seed layer. Lower strain and stress values demonstrate better quality of crystal [43]. The degree of as-grown ZnO nanostructures crystalline alignment can be scrutinized by the texture coefficient derived from Eq. (13) [44, 45].

$$TC_{(h_i k_i l_i)} = \frac{I_{(h_i k_i l_i)}}{I0_{(h_i k_i l_i)}} \left[\frac{1}{N} \sum_{i=1}^{N} \frac{I_{(h_i k_i l_i)}}{I0_{(h_i k_i l_i)}} \right]^{-1} \qquad (13)$$

Eq. (13) explains texture coefficient related to each facet of the ZnO nanostructures. The intensity of the $(h_i k_i l_i)$ plane for standard samples and the intensity of the measured $(h_i k_i l_i)$ lattice plane for prepared samples are depicted by $I0_{(h_i k_i l_i)}$ and $I_{(h_i k_i l_i)}$, while the number of diffraction peaks is demonstrated by N. The unity value of texture coefficient depicts that the sample is aligned like the bulk ZnO. However, increasing or decreasing the mentioned value of texture coefficient has a direct relation with the changes of alignment degree along a specific direction [22]. The calculated texture coefficients are listed in Table 1. It is obvious that the peak intensity of (002) involves higher values which represents perpendicularly growth of ZnO nanostructures on the substrate. Moreover, due to the higher texture coefficient values of (002) plane respect to the non-polar planes, the ZnO NT growth in the direction of [0001] has been occurred.

3.2. Device properties

Two devices of Glass/ITO/AZO/ZnO NR array/MEH-PPV/Al (device A) and Glass/ITO/AZO/ZnO NT array/MEH-PPV/Al (device B) are fabricated by employing NRs and NTs under the circumstances of 90 ˚C, 1 M concentration of KCl solution and 4 h etching time. The spectra of absorbance for ZnO NR/MEH-PPV and ZnO NT/MEH-PPV bi-layers have been

shown in Fig. 6a. The main absorption zone is observed lower than the wavelength of 400 nm. Higher absorbance related to the device (B) stems from its better optical characteristics. Wide area of absorption between 410 to 590 nm originates from MEH-PPV layer. In addition, the optical band gap can be obtained by finding the wavelength of absorption edge (λ_e) calculated by intersecting the linear part of the absorbance spectra with the wavelength axis. From λ_e of 363 nm as well as 371 nm and according to the formula of: $E_g = hc/\lambda_e$ (where h demonstrates the Plank's constant and c depicts the light speed), the optical band gaps are achieved 3.41 and 3.34 eV for device (A) and (B), respectively. Furthermore, to perform a profound review on the defect distribution of both hybrid LEDs, the Urbach energy (E_u) is deduced from the absorbance spectra (α) shown in the inset section of Fig. 6a. According to lambert's law: $I = I_0 e^{-\alpha t}$ (where I_0, I, α and t demonstrate the incident light, the intensity of the beam after transmission through a thickness, absorption coefficient and the thickness of film, respectively) and the definition of absorbance: $A = \log(I/I_0)$, absorption coefficient can be defined by: $\alpha = 2.303A/t$, which A is the absorbance and t displays the film thickness (1.8 μm) [46]. To obtain Urbach energy (E_u) from absorption coefficient, the equation of: $\alpha = \alpha_0 \exp(h\nu/E_u)$ depicts the relation between Urbach energy and α, where α_0 is a constant [47]. As Urbach energy has inverse relationship with the slope of: $ln(\alpha) = ln(\alpha_0) + (h\nu/E_u)$, lower slope of ZnO NR respect to ZnO NT in the inset of Fig. 6a leads to higher value of Urbach energy for ZnO NR (490 meV > 325 meV). As a result, the defect concentration and localized states of ZnO NT is lower than ZnO NR.

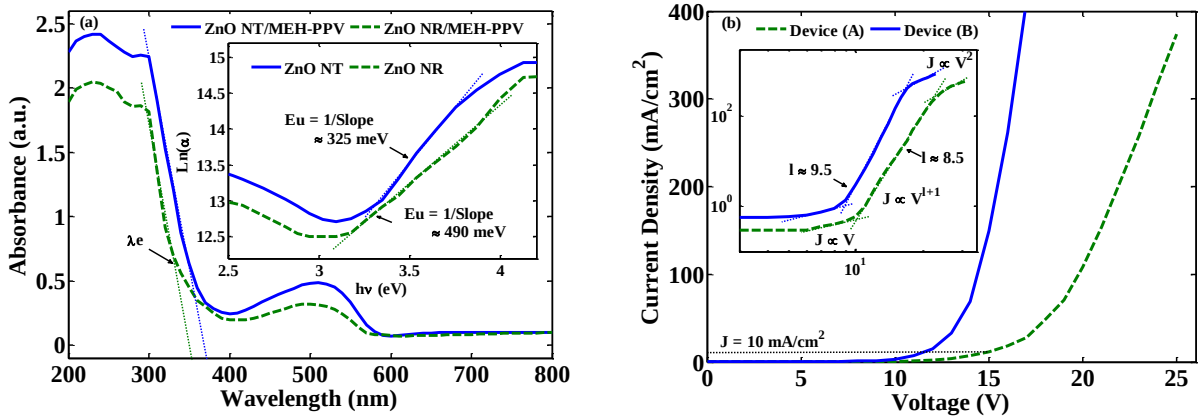

Fig. 6. (a) The absorbance spectra of the layers based on NR/MEH-PPV and NT/MEH-PPV (The inset illustrates relation of $\ln(\alpha)$ and $(h\upsilon)$, (b) Current density vs voltage curve of two devices (The inset depicts logarithmic graph for current density - voltage for two devices).

The current density versus voltage curves of both devices is demonstrated in Fig. 6b. The turn-on voltage related to device based on NR arrays is higher than device based on NT arrays and its value for hybrid LED based on NR and NT equals to 15 and 11.2 V, respectively. According to J-V characteristics of both devices, by applying ZnO NTs as inorganic material, a decline in the turn-on voltage is observed which arises from the lower band gap value of ZnO NTs rather than NRs. The relation between band gap values and turn-on voltages is justified by examining the band diagram of mentioned devices (shown in the inset of Fig. 7b). Higher band gap leads to higher barrier between ITO/AZO contact and ZnO nanostructure layer [10]. Therefore, stronger energy is required to suppress the high hole-injection barrier which leads to higher turn-on voltages. To investigate the hybrid LEDs behavior, the logarithmic plot of the current density versus voltage characteristics for both devices is calculated and compared. From the inset of Fig. 6b, it is evident that at low voltages (first region), both devices show an ohmic behavior that stems from background electrons transportation in accordance with equation of: $J = \sigma V/d$ [48]. Here, the conductivity is illustrated by factor of σ and specimen thickness is shown by d. Second region differs from first one since at medium voltages, J is no longer follow the ohmic behavior and the

power low relation (Mark–Helfrich equation) as: $J \propto V^{l+1}$ becomes dominant which depends on the trapped-controlled space charge-limited conduction model (T-SCLC) [49]. In that case, the current density of devices made from low-mobility MEH-PPV is deduced by Eq. (14) [6, 50]

$$J = q^{1-l} N_v \mu_p \left(\frac{2l+1}{l+1}\right)^{l+1} \left(\frac{l}{l+1}\frac{\varepsilon\varepsilon_0}{N_t}\right)^{l} \frac{V^{l+1}}{d^{2l+1}} \qquad (14)$$

where l is the distribution of traps, q equals to 1.60×10^{-19} c (charge of one electron), μ_{p} is the hole mobility of MEH-PPV, N_v is effective density of states in the valance band of MEH-PPV, N_t is the total concentration of traps, ε_0 is known as permittivity of free space and ε demonstrates the dielectric constant of MEH-PPV. The thickness of the device is defined by d. Furthermore, by increasing the applied voltage and exceeding the trap-filled limit voltage ($V_{TFL} = (N_t q d^2)/(2\varepsilon\varepsilon_0)$), all of the local states are filled by electrons. As a result, there are no available traps left [51]. Accordingly, at higher voltages, Mott-Gurney equation (Child's law) determines the behavior of current density through Eq. (15) [52, 53]:

$$J = (9\mu\varepsilon_0\varepsilon_r v^2)/(8l^3) \qquad (15)$$

The total concentration of traps (N_t) for both hybrid LEDs is calculated by Eq. (14). The calculated N_t for device (A) is $3.92 \times 10^{14}\ cm^{-3}$ and for device (B) is $2.39 \times 10^{14}\ cm^{-3}$. Based on the inset of Fig. 6b, the distribution of traps (l) is obtained from the logarithmic curve of J-V and equals to 8.5 and 9.5 for devices based on ZnO NR and ZnO NT, respectively. The characteristic temperature (T_t) is derived by: $T_t = l \times T$ (T is ambient temperature of 300 K) which is equal to 2550 and 2850 K for device (A) and (B). Moreover, the characteristic energies (E_B) of two devices (A and B) can be obtained by: $E_B = K_B \times T_t$ (K_B depicts Boltzmann constant) which are equal to 0.22 and 0.24 eV, respectively [54]. The trap concentration related to device based on NR is lower than NT which arises from lower crystalline imperfection of device (B) respect to the device (A).

The photoluminescence (PL) spectra for the samples of ZnO NR and ZnO NT with the optimal etching condition is illustrated in Fig. 7a. Due to the ZnO wide band gap, free-excitonic near band emission (NBE) is appeared with an intense peak at 372 and 378 nm for ZnO NR and NT, respectively [55]. Burstein–Moss (BM) effect causes a slight red shift of ZnO NT with respect to ZnO NR in the PL spectra which stems from occupying the low states located at the conduction band with higher electron concentration and forcing the valence band electrons to move toward the high states of the conduction band [56, 57]. Besides, because of some imperfections including oxygen vacancy (V_O^+), zinc vacancy (V_{Zn}), anti-site defect (O_{Zn}), and interstitial oxygen (O_i^-) which is found in ZnO nanostructures, a broad green-yellowish emission from 450 to 800 nm as deep level emission (DLE) is observed for samples [58, 59]. Moreover, NBE to DLE ratio expresses the quality of ZnO nanostructures and higher I_{NBE}/I_{DLE} leads to higher crystal quality [47]. The ZnO NT based device has maximum I_{NBE}/I_{DLE} ratio of 6 which illustrates the superior quality of crystal. The defect concentration in the center of ZnO NR are higher than NT. By etching the (002) polar planes in ZnO NT, the trap concentration in the center becomes lower which results in the lower defect emission and higher I_{NBE}/I_{DLE} ratio in PL spectra [60]. The obtained results are in agreement with lower Urbach energy and lower total trap concentration of device (B) in comparison with device (A) which discussed former.

According to Fig. 7b, the EL spectra for device (A) and (B) is studied and compared. Near-band emission arising from free-excitonic emission is also observed in the EL spectra which is more intense than other peaks. Due to the difference of NRs and NTs' band gap, EL spectra for device (B) shifts toward the larger wavelengths (red shift) [10]. Besides, many parameters involving lattice strains, crystallographic defects, electron-phonon couplings, linear dislocations and interface imperfections induce a phenomenon known as Stokes shift [61]. The Stokes shift describes the difference between NBE peaks of EL and PL spectra [62]. In addition, broad area from 577 to 635 nm with a main peak at 590 nm originate from vibrionic-transition of MEH-PPV

layer and point defects within ZnO nanostructures (such as V_O, O_i and V_OZn_i cluster) [48]. The higher EL intensity of device (B) is a confirmation of lower Urbach energy of device (B). Subsequently, since ZnO NT based device has fewer defects, more charge carriers (electrons as well as holes) are capable of participating in inter-band transition or in radiative emission.

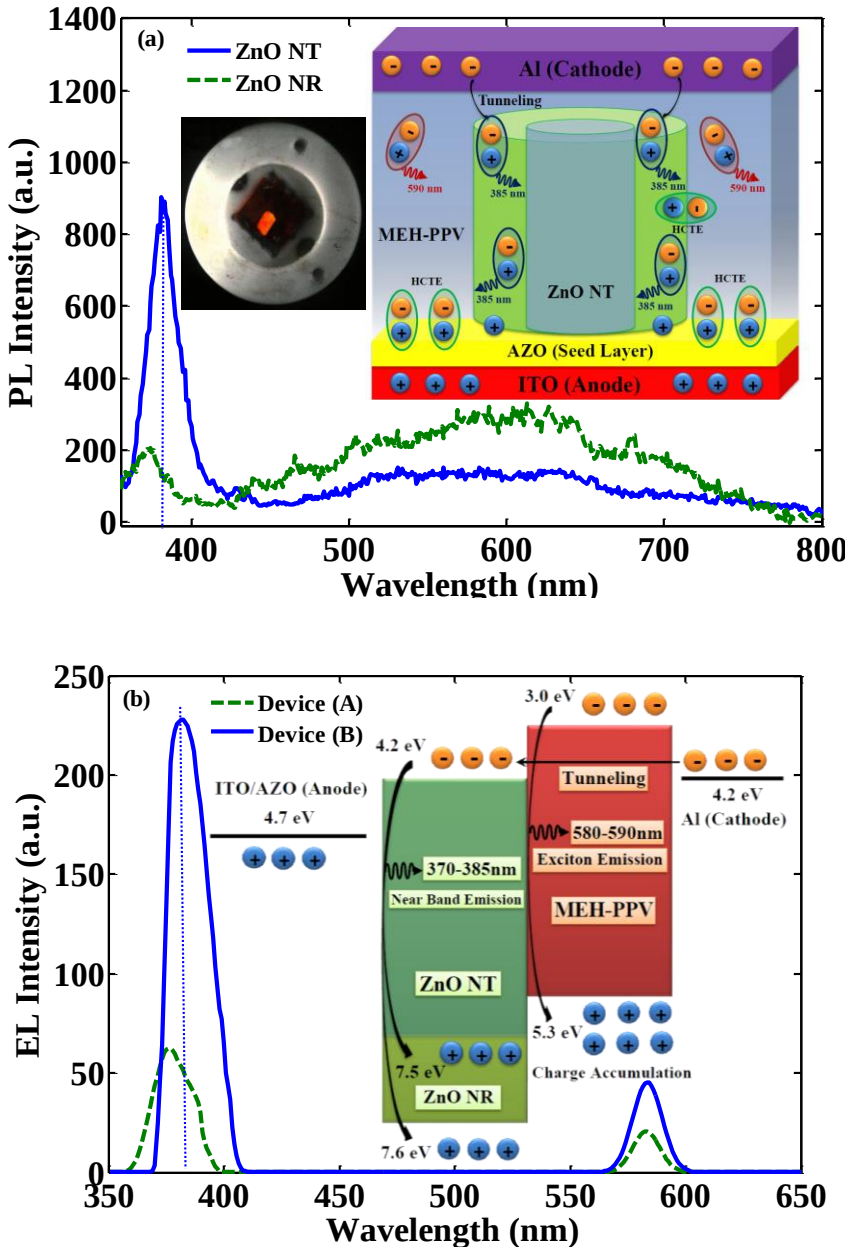

Fig. 7. (a) Photoluminescence (PL) spectra of the ZnO NR and the optimal ZnO NT (The insets depict the opto-electronic mechanism of the structure and the visible orange-red luminescence of the fabricated device), (b) Electroluminescence (EL) spectra of two structures (The inset shows the diagram of energy band).

For more in-depth investigation of light generation mechanism, the generation of light is considered and studied for both devices. From insets of Fig. 7a and 7b, Al is the source of electrons that moves the electrons toward the MEH-PPV and on the other side, holes are injected into the organic layer from ITO/AZO anode through the ZnO nanostructures. As the MEH-PPV's mobility for minority carriers is much lower than ZnO nanostructures' one, electrons flow slowly within the MEH-PPV layer, while holes are passed away from ZnO with higher rate of speed. As a result, carriers recombine perfectly in MEH-PPV layer at lower voltages and excitonic light which is emitted at the wavelength of 590 nm appears (see the inset of Fig. 7a). However, by increasing the voltage, the band bending and tunneling of carriers are occurred which leads to band-to-band transition and the free carriers which are recombining in the ZnO nanostructures create near UV light at the wavelengths of 380 and 385 nm for device (A) and (B), respectively [48]. In that situation, more electrons tunnel to the conduction band of ZnO nanostructures without flowing within the MEH-PPV layer and recombine with holes injected from ITO/AZO anode to the ZnO nanostructures' valence band which lead to near UV band edge emission (see inset of Fig. 7a). Between valance band of ZnO and MEH-PPV's HOMO level, an adequate barrier collects and confines the holes in the inorganic layer which helps to NBE. Moreover, since LUMO level of organic layer is higher than the conduction band of inorganic layer and conversely, the valence band of the inorganic layer is lower than the HOMO level of the organic layer, not only the dominant emission is the band edge emission, but also the intensity of UV emission at 380 nm is sharper than excitonic emission at 590 nm [14]. According to the differences of band alignment between two devices based on ZnO NR and ZnO NT, it is obvious that hole injection barrier for device (B) is lower than device (A), therefore, less energy is required to concur the barrier results in the reduction in turn-on voltage. It is noteworthy that, under reverse biases, because of the confinement effect of electrons in the ZnO nanostructure and holes in MEH-PPV layer, any type of emission is implausible. In that case, since the LUMO level of organic layer is located above

the ZnO's conduction band and ZnO's valence band is located under the HOMO of organic layer, electrons and holes are not capable of moving to higher and lower potentials, respectively and light cannot be released under reverse bias (see inset of Fig. 7b) [63]. There are other factors except free carrier recombination which might enhance the UV emission. First factor is the Wannier-Mott excitons within the ZnO with binding energy of 60 meV which are active in the room temperature and might boost the near violate emission in high voltages [64]. Second, the energy exchange between the Frenkel and Wannier-Mott excitons from MEH-PPV to ZnO NT due to the narrow distance between organic and inorganic layer (1-2 nm) might lead to more intense UV emission at high electric fields (see inset of Fig. 7a) [65, 66]. Moreover, hybrid charge-transfer excitons (HCTE) usually create in I/O interfaces [67]. The HCTEs transfer a charge from one atom to another one in the organic and inorganic layers and despite Frankel and Wannier-Mott excitons, they illustrate a static electric dipole moment [68]. Nevertheless, the HCTEs are commonly non-radiative triplet excitons [66, 67] and do not affect the EL spectra since there is no exciplex emission at the infrared range of the device (A) or (B).

3.3. Waveguiding effects of the proposed devices

Since the refractive index of the ZnO NR or ZnO NT is higher than MEH-PPV (2.04 > 1.5) [69], the ZnO nanostructures act as core and MEH-PPV behaves as cladding in device (A) and (B). To determine whether the generated UV-light in both devices can be guided through the ZnO core or not, the maximum propagation angle must be calculated. The maximum propagation angle of the light in the waveguide can be deduced by Snell's law [69, 70]:

$$n_1 \sin(\theta_1) = n_2 \sin(\theta_2) \qquad (16)$$

where n_1 and n_2 are the refractive index of the core (ZnO NRs) and cladding (MEH-PPV) which are equal to 2.04 and 1.5, respectively [69]. The maximum propagation angle of the light in the ZnO core (θ_1) can be calculated if θ_2 supposed to be 90 °. According to Fig. 8a and Eq. 16, if the

angle of the emitted light in the ZnO becomes less than 42.6º respect to the propagation axis (Z-axis), the emitted light capture and guide within the ZnO core. Now the chief question is: "For the propagation angles less than 42.6º, which one of the devices based on ZnO NR and NT can guide and extract the light from the UV-OLED more efficiently and coherently with minimum reflection from the substrate?". For analyzing the light extraction and the effect of ZnO NR and NT on the intensity of the near UV peaks in EL spectra (Fig. 7b), the waveguide's capability of light capturing (waveguide parameter) for ZnO NR can be obtained by Eq. (17) [1, 2, 71]:

$$V = \frac{2\pi a}{\lambda}\sqrt{n_1^2 - n_2^2} \qquad (17)$$

where a depicts the average radius of ZnO NRs (200 nm) and λ demonstrates the wavelength of the UV light extracted from the EL spectra (380 nm). Furthermore, the numerical aperture of waveguide can be defined as: $N.A. = \sqrt{n_1^2 - n_2^2}$. As the calculated waveguide parameter for device (A) is 4.572 which is higher than the cut-off frequency of transverse electric (TE) mode of TE_{01} for standard step-index waveguide (2.405) [72], the device based on ZnO NR are not capable for supporting the single-mode propagation and light passes through the device (A) with multi-modes [69]. With the linear polarization (LP) assumption and simplification, four modes including LP_{01}, LP_{02}, LP_{11} and LP_{21} can be guided in the device with ZnO NR structure [73]. Moreover, from Fig. 8a, it is obvious that the collision and interference between the modes reduces the intensity of the extracted light results in lower UV peak of device (A) in EL spectra.

On the other side, since the ZnO NT has a ring-core (annular or tubular) shape, the waveguide parameter determines slightly different. Conventional ring-core waveguides are constraining from inner (a) and outer (b) radiuses. Accordingly, the waveguide parameter can be deduced by Eq. (18) [74-76]:

$$V = \frac{2\pi(b-a)}{\lambda}\sqrt{n_1^2 - n_2^2} \qquad (18)$$

where λ is the wavelength of the propagated light from device (B) extracted from the EL spectra (385 nm). In ring-core waveguides, the ratio between inner and outer radius (ρ) determines the cut-off frequency. In device (B), this ratio is 0.5 since the average inner and outer radiuses are 100 and 200 nm, respectively (see Fig. 8a). The relation between cut-off frequencies and ρ parameter in ring-core waveguides has been calculated in many works [72, 74, 76]. For the ρ parameter equals to 0.5, the cut-off frequency of TE_{01} mode is 2.554 [72]. It means that if the waveguide parameter of ring-core fiber is less than 2.554, the waveguide propagates single-fundamental-mode. Since the calculated waveguide factor for ZnO NT structure is 2.255 which is lower than 2.554, device (B) propagates coherent, co-phase and uniform single-mode light (see Fig. 8a). Due to the single-mode propagation of device (B), maximum number of photons can be extracted from ZnO/MEH-PPV emissive interface and directed vertically towards the ITO layer which enhances the EL intensity of device (B). Moreover, the reflection from the ITO/AZO substrate can be acquired from: $r = (n_1 - n_2)/(n_1 + n_2)$; which n_1 and n_2 are the refractive index of AZO and ITO layers, respectively [69]. The calculations show that there is almost no back reflection from the ITO/AZO substrate since the refractive index of ITO is equal to 2.06 which is close to AZO layer [69].

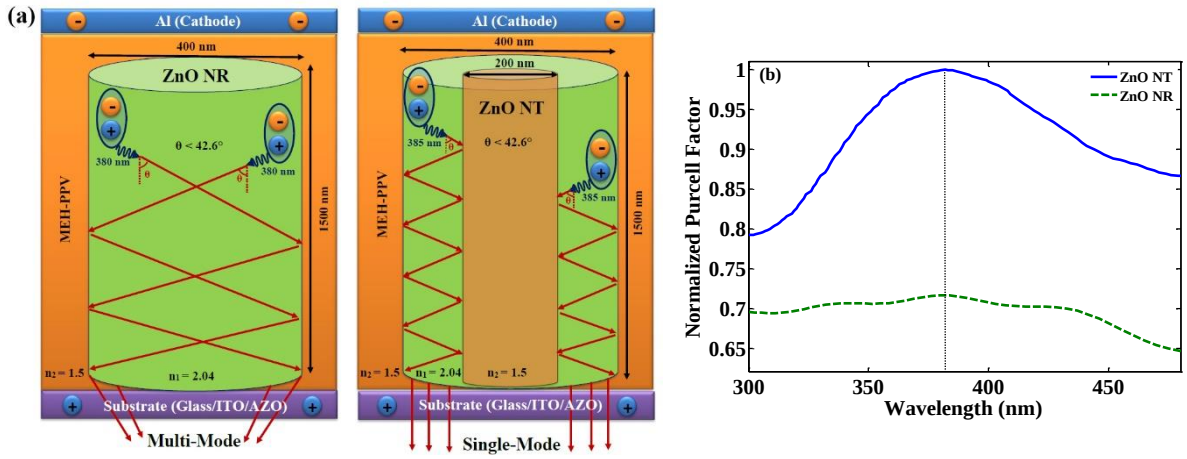

Fig. 8. (a) The waveguiding mechanism of the devices; (b) The normalized Purcell factor spectra of the ZnO NR and ZnO NT.

To illustrate the dependence of ZnO nanostructure's shape on the amplification of the spontaneous emission (Purcell effect) [77], radiative recombination rate and the electric field distribution in cavity, two simulations based on Lumerical FDTD solution and Silvaco TCAD software have been performed. The input parameters utilized in the simulations are depicted in Table 2.

Table 2. Parameters used in Silvaco TCAD and Lumerical FDTD simulations.

	Units	**ZnO Nanorod**	**ZnO Nanotube**	**MEH-PPV**
Aspect Ratio or Thickness	nm	1500/400	1500/400	1600
Doping	cm^{-3}	1e18	1e18	1e15
Band Gap Energy (E_g)	eV	3.26-3.41	3.22-3.34	2.3
Electron Affinity (χ)	eV	4.2	4.2	3.0
Permittivity	--	8.5	8.5	3
Electron Mobility (μ_n)	$cm^2/V.s$	100	100	0.5e-5
Hole Mobility (μ_p)	$cm^2/V.s$	25	25	0.5e-4
Effective Density of States for Electrons (N_c)	cm^{-3}	2.2e18	2.2e18	1e21
Effective Density of States for Electrons (N_v)	cm^{-3}	1.8e19	1.8e19	1e21
Refractive Index	--	2.04	2.04	1.5
References	--	[61, 69]	[60, 69]	[61, 62, 69]
Electrodes	**Units**		**Al**	**ITO**
Thickness	nm		100	100
Work Function (ϕ)	eV		4.2	4.7
References	--		[63]	[69]

The method for measuring the Purcell factor (PF) which in that case the dipole is resonant with cavity can be obtained by Eq. (19) [78]:

$$PF = \frac{3}{4\pi^2}\left(\frac{\lambda}{n}\right)^3 \frac{Q}{V_{mode}} \quad (19)$$

where λ describes the wavelength of the dipole and n shows the refractive index. Q is the quality factor and V_{mode} is the mode volume calculated using Eq. (20) [79]:

$$V_{mode} = \int_V \varepsilon(r)\,|E(r)|^2 d^3r / max(\varepsilon(r)|E(r)|^2) \quad (20)$$

where ε(r) is the material permittivity and $E(r)$ is local electric field at radius of r. According to the normalized Purcell factor illustrated in Fig. 8b, the peak at the wavelength of 385 nm in ZnO NT is distinguished which means that the emitted UV light perfectly coupled with the fundamental mode of ZnO NT ring-core waveguide and leads to higher efficiency. Besides, there is almost no peak for ZnO NR in UV region which confirms the multi-mode propagation of ZnO NR waveguide. To better understanding of the light intensification mechanism, the radiative recombination rates of both devices are simulated and illustrated in Figs. 9a and 9b.

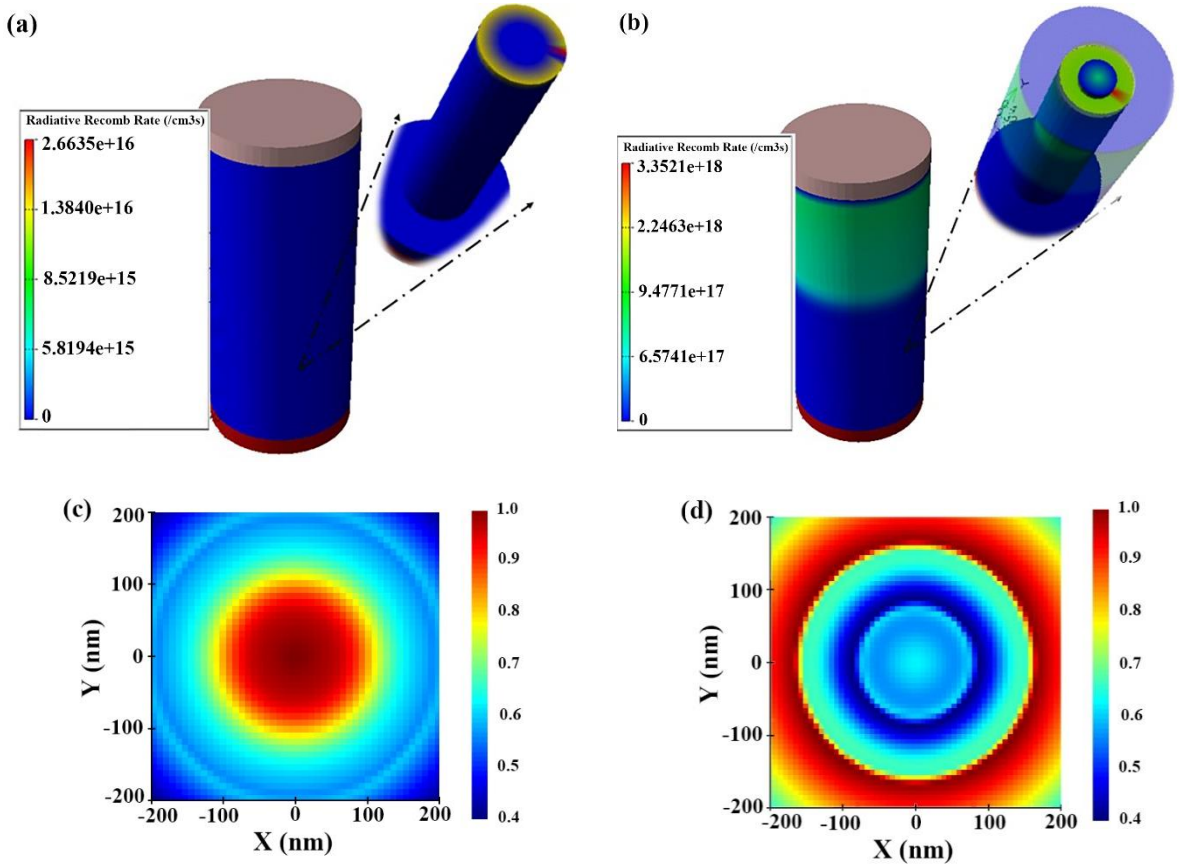

Fig. 9. Radiative recombination rate of the devices with (a) ZnO NR and (b) ZnO NT; The intensity of the electric field in (c) ZnO NR and (d) ZnO NT structures.

According to the Fig. 9a, relatively weak emission in the order of $10^{16}/cm^3s$ can be seen at the ZnO NR's external wall and its interface with MEH-PPV layer. However, higher surface-to-

volume ratio of ZnO NTs respect to ZnO NR leads to stronger optically active recombination rate at ZnO NT/MEH-PPV interface in the order of $10^{18}/cm^3s$ which causes more intense UV emission [10] (depicted in Fig. 9b). To calculate the electric field distribution in the cavity, it is important to investigate the discrete Fourier transform (DFT) algorithm, which the time domain electric field (E) can be considered as Eq. (21) [79]:

$$\hat{E}(f) = \int_{-\infty}^{+\infty} E(t)e^{-j\omega t}dt \approx \Delta t \sum_{n=0}^{N-1} E(n\Delta t)\, e^{-j\omega n\Delta t} \qquad (21)$$

where N describes the length of the time domain sequence, ω is angular frequency which equals to $2\pi f$ and f shows the desired frequency and j is $\sqrt{-1}$. According to Figs. 9c and 9d, the dipole source is utilized and electric field distribution and waveguide emission can be achieved by the radiation properties of the mentioned dipole source. The electric field can be defined by an electric dipole as: $E = E^0 + E^r$, which E^0 demonstrates the electric field of dipole in the infinite medium and E^r explains the reflected field from nanostructures' interface [80, 81]. There is strong electric field distribution in the width of ZnO NT which confirms the efficient propagation of the UV light in ZnO NT ring-core waveguide. The electric field intensity distribution of the radial modes (RM) shows that in the case of ZnO NR the coupled light is in the center and can easily scape from ZnO NR structure, while the light escapes from the ZnO NT more slowly [82, 83].

4. Conclusions

This work investigates the effect of applying ZnO NTs as a single-mode ring-core waveguide on the optical and electrical features of OLEDs in near UV range. First of all, ZnO NRs have been grown via CBD technique and have been converted to ZnO NT via various etching solution concentration, etching time and etching temperature. In the following, the impact of both ZnO NR and ZnO NT arrays on two hybrid LEDs with the structures of ITO/AZO/ZnO NR array/MEH-

PPV/Al and ITO/AZO/ZnO NT array/MEH-PPV/Al have been investigated. According to the current density-voltage curve, device based on ZnO NT exhibits lower turn-on voltage related to lower band gap of ZnO NTs. Furthermore, the device based on ZnO NT arrays serves several benefits including lower Urbach energy and defect emission, lower trap concentration, higher radiative recombination rate and higher UV peak in PL and EL spectra. The waveguide parameter for ZnO NT ring-core structure is less than the cut-off frequency of TE_{01} mode ($2.255 < 2.554$) which results in single-mode propagation. In contrast, ZnO NR based device depicts multi-mode propagation. Furthermore, the normalized Purcell factor of ZnO NT based device shows a peak at wavelength of 385 nm which indicates that the emitted UV light from OLED is perfectly coupled with the fundamental mode of ring-core waveguide, but there is almost no peak for ZnO NR in UV range. Consequently, ZnO NT-based device supports single-mode propagation with high electric field distribution in the wall which causes more intense UV peak in EL spectra with superior light outcoupling. We believe that this work can become a great breakthrough in lighting industry and UV applications.

References

[1] S. Chen, M.-P. Zhuo, X.-D. Wang, G.-Q. Wei, and L.-S. Liao, "Optical waveguides based on one-dimensional organic crystals," *PhotoniX*, vol. 2, pp. 1-24, 2021.

[2] S. K. Selvaraja and P. Sethi, "Review on optical waveguides," *Emerging Waveguide Technology*, vol. 95, 2018.

[3] J. Liu, G. Zhu, J. Zhang, Y. Wen, X. Wu, Y. Zhang, Y. Chen, X. Cai, Z. Li, and Z. Hu, "Mode division multiplexing based on ring core optical fibers," *IEEE Journal of Quantum Electronics*, vol. 54, pp. 1-18, 2018.

[4] K. Mistewicz, W. Matysiak, M. Jesionek, P. Jarka, M. Kępińska, M. Nowak, T. Tański, D. Stróż, J. Szade, and K. Balin, "A simple route for manufacture of photovoltaic devices based on chalcohalide nanowires," *Applied Surface Science*, vol. 517, p. 146138, 2020.

[5] A. Stanculescu, C. Breazu, M. Socol, O. Rasoga, N. Preda, G. Petre, A. Solonaru, M. Grigoras, F. Stanculescu, and G. Socol, "Effect of ITO electrode patterning on the properties of organic heterostructures based on non-fullerene acceptor prepared by MAPLE," *Applied Surface Science*, vol. 509, p. 145351, 2020.

[6] M. N. Rezaie, S. Mohammadnejad, and S. Ahadzadeh, "Hybrid inorganic-organic light-emitting heterostructure devices based on ZnO," *Optics & Laser Technology,* vol. 138, p. 106896, 2021.
[7] A. Salem, S. El-Sheikh, F. A. Harraz, S. Ebrahim, M. Soliman, H. Hafez, I. Ibrahim, and M. Abdel-Mottaleb, "Inverted polymer solar cell based on MEH-PPV/PC61BM coupled with ZnO nanoparticles as electron transport layer," *Applied Surface Science,* vol. 425, pp. 156-163, 2017.
[8] M. N. Rezaie, N. Manavizadeh, E. Nadimi, and F. A. Boroumand, "Quality enhancement of AZO thin films at various thicknesses by introducing ITO buffer layer," *Journal of Materials Science: Materials in Electronics,* vol. 28, pp. 9328-9337, 2017.
[9] V. V. Multian, A. V. Uklein, A. N. Zaderko, V. O. Kozhanov, O. Y. Boldyrieva, R. P. Linnik, V. V. Lisnyak, and V. Y. Gayvoronsky, "Synthesis, characterization, luminescent and nonlinear optical responses of nanosized ZnO," *Nanoscale research letters,* vol. 12, pp. 1-8, 2017.
[10] S. Mohammadnejad, S. Ahadzadeh, and M. N. Rezaie, "Effect of ZnO nanorods and nanotubes on the electrical and optical characteristics of organic and perovskite light-emitting diodes," *Nanotechnology,* vol. 32, p. 245204, 2021.
[11] M. Caglar, S. Ilican, Y. Caglar, and F. Yakuphanoglu, "Electrical conductivity and optical properties of ZnO nanostructured thin film," *Applied surface science,* vol. 255, pp. 4491-4496, 2009.
[12] M. N. Rezaie and S. Mohammadnejad, "Effect of the PEDOT: PSS buffer layer on the performance of hybrid ZnO nanorods/polymer electroluminescent diode," *Optical and Quantum Electronics,* vol. 52, pp. 1-14, 2020.
[13] D. Hewidy, A.-S. Gadallah, and G. A. Fattah, "Hybrid electroluminescent device based on MEH-PPV and ZnO," *Physica B: Condensed Matter,* vol. 507, pp. 46-50, 2017.
[14] S.-L. Zhao, P.-Z. Kan, Z. Xu, C. Kong, D.-W. Wang, Y. Yan, and Y.-S. Wang, "Electroluminescence of ZnO nanorods/MEH-PPV heterostructure devices," *Organic Electronics,* vol. 11, pp. 789-793, 2010.
[15] A. Ng, X. Chen, F. Fang, Y. Hsu, A. Djurišić, C. Ling, H. L. Tam, K. W. Cheah, P. Fong, and H. Lui, "Solution-based growth of ZnO nanorods for light-emitting devices: hydrothermal vs. electrodeposition," *Applied Physics B,* vol. 100, pp. 851-858, 2010.
[16] D.-J. Yun, H. Ra, J.-M. Kim, S. Jeon, S. H. Park, M. Seol, and S. Lee, "Well-aligned ZnO nanorod array covered with ruthenium layers for alternative counter electrodes in dye-sensitized solar cells," *Applied Surface Science,* vol. 550, p. 149273, 2021.
[17] M. Abdelfatah and A. El-Shaer, "One step to fabricate vertical submicron ZnO rod arrays by hydrothermal method without seed layer for optoelectronic devices," *Materials Letters,* vol. 210, pp. 366-369, 2018.
[18] A. El-Shaer, M. Abdelfatah, A. Basuni, and M. Mosaad, "Effect of KOH molarity and annealing temperature on ZnO nanostructure properties," *Chinese journal of physics,* vol. 56, pp. 1001-1009, 2018.
[19] S. C. Lyu, Y. Zhang, C. J. Lee, H. Ruh, and H. J. Lee, "Low-temperature growth of ZnO nanowire array by a simple physical vapor-deposition method," *Chemistry of materials,* vol. 15, pp. 3294-3299, 2003.
[20] A. Hassanpour, N. Bogdan, J. A. Capobianco, and P. Bianucci, "Hydrothermal selective growth of low aspect ratio isolated ZnO nanorods," *Materials & Design,* vol. 119, pp. 464-469, 2017.
[21] Y. Li, J. Feng, Y. Wang, B. He, Y. Zhao, C. Xu, and J. Wang, "Highly conductive and flexible electrodes based on ultrathin aluminum-doped zinc oxide epitaxial films," *Applied Surface Science,* p. 150925, 2021.

[22] M. N. Rezaie, N. Manavizadeh, F. D. Nayeri, M. M. Bidgoli, E. Nadimi, and F. A. Boroumand, "Effect of seed layers on low-temperature, chemical bath deposited ZnO nanorods-based near UV-OLED performance," *Ceramics International,* vol. 44, pp. 4937-4945, 2018.
[23] L. Schlur, J. R. Calado, and D. Spitzer, "Synthesis of zinc oxide nanorods or nanotubes on one side of a microcantilever," *Royal Society open science,* vol. 5, p. 180510, 2018.
[24] Y. Zhang, M. Liu, W. Ren, and Z.-G. Ye, "Well-ordered ZnO nanotube arrays and networks grown by atomic layer deposition," *Applied Surface Science,* vol. 340, pp. 120-125, 2015.
[25] S. Mohammadnejad, S. Ahadzadeh, and M. N. Rezaie, "Tunable band gap energy of single-walled zigzag ZnO nanotubes as a potential application in photodetection," *Current Applied Physics,* vol. 29, pp. 138-147, 2021.
[26] J. R. Sadaf, M. Q. Israr, S. Kishwar, O. Nur, and M. Willander, "White electroluminescence using ZnO nanotubes/GaN heterostructure light-emitting diode," *Nanoscale research letters,* vol. 5, pp. 957-960, 2010.
[27] H. Dong, J. Zhou, and S. Virtanen, "Fabrication of ZnO nanotube layer on Zn and evaluation of corrosion behavior and bioactivity in view of biodegradable applications," *Applied Surface Science,* vol. 494, pp. 259-265, 2019.
[28] P. Limnonthakul, D. Yangnoi, P. Bintachitt, M. Hengwattana, and M. Horprathum, "Influence of Various Precursor Compositions and Substrate Angles on ZnO Nanorod Morphology Growth by Aqueous Solution Method," *JOURNAL OF MATHEMATICAL AND FUNDAMENTAL SCIENCES,* vol. 48, pp. 48-54, 2016.
[29] A. Thankappan, S. Thomas, and V. Nampoori, "Tuning the face orientation of ZnO nano/microcrystals by a wet chemical method," *Chinese Optics Letters,* vol. 11, p. 101801, 2013.
[30] A. Van der Drift, "Evolutionary selection, a principle governing growth orientation in vapour-deposited layers," *Philips Res. Rep,* vol. 22, pp. 267-88, 1967.
[31] Q. Ahsanulhaq, A. Umar, and Y. Hahn, "Growth of aligned ZnO nanorods and nanopencils on ZnO/Si in aqueous solution: growth mechanism and structural and optical properties," *Nanotechnology,* vol. 18, p. 115603, 2007.
[32] Y. Chen, Q. Qiao, Y. Liu, and G. Yang, "Size-controlled synthesis and optical properties of small-sized ZnO nanorods," *The Journal of Physical Chemistry C,* vol. 113, pp. 7497-7502, 2009.
[33] P. Giri, S. Dhara, and R. Chakraborty, "Effect of ZnO seed layer on the catalytic growth of vertically aligned ZnO nanorod arrays," *Materials Chemistry and Physics,* vol. 122, pp. 18-22, 2010.
[34] M. Poornajar, P. Marashi, D. H. Fatmehsari, and M. K. Esfahani, "Synthesis of ZnO nanorods via chemical bath deposition method: The effects of physicochemical factors," *Ceramics International,* vol. 42, pp. 173-184, 2016.
[35] B. Weintraub, Y. Deng, and Z. L. Wang, "Position-controlled seedless growth of ZnO nanorod arrays on a polymer substrate via wet chemical synthesis," *The Journal of Physical Chemistry C,* vol. 111, pp. 10162-10165, 2007.
[36] M. Abdelfatah, W. Ismail, and A. El-Shaer, "Low cost inorganic white light emitting diode based on submicron ZnO rod arrays and electrodeposited Cu2O thin film," *Materials Science in Semiconductor Processing,* vol. 81, pp. 44-47, 2018.
[37] M. F. Malek, M. H. Mamat, T. Soga, S. A. Rahman, S. A. Bakar, A. S. Ismail, R. Mohamed, S. A. Alrokayan, H. A. Khan, and M. R. Mahmood, "Thickness-controlled synthesis of vertically aligned c-axis oriented ZnO nanorod arrays: Effect of growth time via novel dual sonication sol–gel process," *Japanese Journal of Applied Physics,* vol. 55, p. 01AE15, 2015.

[38] L. Shi, Y. Xu, and Q. Li, "Shape-selective synthesis and optical properties of highly ordered one-dimensional ZnS nanostructures," *Crystal Growth and Design,* vol. 9, pp. 2214-2219, 2009.
[39] D. Solís-Cortés, F. Martín, R. Schrebler, E. Navarrete-Astorga, M. C. López-Escalante, J. Peinado-Pérez, J. R. Ramos-Barrado, and E. A. Dalchiele, "Electrochemical Growth of ZnO Nanorod Arrays onto Transparent Conductive IZO: Ga Substrates," *Journal of The Electrochemical Society,* vol. 167, p. 112504, 2020.
[40] A. Kumar, G. Malik, A. Kumar, R. Chandra, and R. S. Mulik, "Transformation nanorod to nanotube of highly oriented novel h-BN hierarchical nanostructured arrays synthesized via two-step wet chemical route," *Materials Characterization,* vol. 171, p. 110820, 2021.
[41] Y. Wang, S. P. Lau, H. Lee, S. F. Yu, B. Tay, X. Zhang, K. Tse, and H. Hng, "Comprehensive study of ZnO films prepared by filtered cathodic vacuum arc at room temperature," *Journal of applied physics,* vol. 94, pp. 1597-1604, 2003.
[42] M. Abdelfatah, H. Salah, M. El-Henawey, A. Oraby, A. El-Shaer, and W. Ismail, "Insight into Co concentrations effect on the structural, optical, and photoelectrochemical properties of ZnO rod arrays for optoelectronic applications," *Journal of Alloys and Compounds,* vol. 873, p. 159875, 2021.
[43] B. Zhu, J. Wang, S. Zhu, J. Wu, D. Zeng, and C. Xie, "Thickness study of AZO films by RF sputtering in Ar+ H2 atmosphere at room temperature," *physica status solidi (a),* vol. 209, pp. 1251-1258, 2012.
[44] M. Kumar, A. Kumar, and A. Abhyankar, "Influence of texture coefficient on surface morphology and sensing properties of w-doped nanocrystalline tin oxide thin films," *ACS applied materials & interfaces,* vol. 7, pp. 3571-3580, 2015.
[45] Y. Wang, W. Tang, and L. Zhang, "Crystalline size effects on texture coefficient, electrical and optical properties of sputter-deposited Ga-doped ZnO thin films," *Journal of Materials Science & Technology,* vol. 31, pp. 175-181, 2015.
[46] D. F. Swinehart, "The beer-lambert law," *Journal of chemical education,* vol. 39, p. 333, 1962.
[47] M. Malek, M. Mamat, M. Musa, Z. Khusaimi, M. Sahdan, A. Suriani, A. Ishak, I. Saurdi, S. Rahman, and M. Rusop, "Thermal annealing-induced formation of ZnO nanoparticles: Minimum strain and stress ameliorate preferred c-axis orientation and crystal-growth properties," *Journal of Alloys and Compounds,* vol. 610, pp. 575-588, 2014.
[48] M. N. Rezaie, N. Manavizadeh, E. M. N. Abadi, E. Nadimi, and F. A. Boroumand, "Comparison study of transparent RF-sputtered ITO/AZO and ITO/ZnO bilayers for near UV-OLED applications," *Applied Surface Science,* vol. 392, pp. 549-556, 2017.
[49] J. A. Röhr, X. Shi, S. A. Haque, T. Kirchartz, and J. Nelson, "Charge transport in spiro-OMeTAD investigated through space-charge-limited current measurements," *Physical review applied,* vol. 9, p. 044017, 2018.
[50] S. Jain, A. K. Kapoor, W. Geens, J. Poortmans, R. Mertens, and M. Willander, "Trap filled limit of conducting organic materials," *Journal of applied physics,* vol. 92, pp. 3752-3754, 2002.
[51] A. Kumar, A. Singh, S. Samanta, R. Prasad, A. Debnath, D. Aswal, and S. Gupta, "Trap free space charge limited conduction and high mobility in cobalt phthalocyanine-iron phthalocyanine composite thin films," in *Solid State Phenomena,* 2014, pp. 52-56.
[52] S. Rutledge and A. Helmy, "Carrier mobility enhancement in poly (3, 4-ethylenedioxythiophene)-poly (styrenesulfonate) having undergone rapid thermal annealing," *Journal of Applied Physics,* vol. 114, p. 133708, 2013.
[53] M. Zaini, M. M. Sarjidan, and W. A. Majid, "Determination of Traps' Density of State in OLEDs from Current–Voltage Analysis," *Chinese Physics Letters,* vol. 33, p. 018101, 2016.

[54] M. Rafiq, Y. Tsuchiya, H. Mizuta, S. Oda, S. Uno, Z. Durrani, and W. Milne, "Charge injection and trapping in silicon nanocrystals," *Applied Physics Letters*, vol. 87, p. 182101, 2005.
[55] S. Iwan, J. Zhao, S. Tan, and X. Sun, "Enhancement of UV photoluminescence in ZnO tubes grown by metal organic chemical vapour deposition (MOCVD)," *Vacuum*, vol. 155, pp. 408-411, 2018.
[56] S.-M. Park, T. Ikegami, K. Ebihara, and P.-K. Shin, "Structure and properties of transparent conductive doped ZnO films by pulsed laser deposition," *applied surface science*, vol. 253, pp. 1522-1527, 2006.
[57] J. Lu, Z. Ye, Y. Zeng, L. Zhu, L. Wang, J. Yuan, B. Zhao, and Q. Liang, "Structural, optical, and electrical properties of (Zn, Al) O films over a wide range of compositions," *Journal of Applied Physics*, vol. 100, p. 073714, 2006.
[58] S. Arya, S. S. Danewalia, M. Arora, and K. Singh, "Effect of variable oxidation states of vanadium on the structural, optical, and dielectric properties of B2O3–Li2O–ZnO–V2O5 glasses," *The Journal of Physical Chemistry B*, vol. 120, pp. 12168-12176, 2016.
[59] M. Willander, O. Nur, J. R. Sadaf, M. I. Qadir, S. Zaman, A. Zainelabdin, N. Bano, and I. Hussain, "Luminescence from zinc oxide nanostructures and polymers and their hybrid devices," *Materials*, vol. 3, pp. 2643-2667, 2010.
[60] F. Karegar, M. Kolahdouz, F. D. Nayeri, R. Soleimanzadeh, M. Hosseini, Z. K. Esfahani, and K. Zhang, "Light-Emitting n-ZnO Nanotube/n+-GaAs Heterostructures Processed at Low Temperatures," *IEEE Photonics Technology Letters*, vol. 27, pp. 1430-1433, 2015.
[61] M. Alauddin, J. K. Song, and S. M. Park, "Effects of aluminum doping and substrate temperature on zinc oxide thin films grown by pulsed laser deposition," *Applied Physics A*, vol. 101, pp. 707-711, 2010.
[62] B. Ullrich, A. K. Singh, P. Barik, H. Xi, and M. Bhowmick, "Inherent photoluminescence Stokes shift in GaAs," *Optics letters*, vol. 40, pp. 2580-2583, 2015.
[63] D.-W. Wang, S.-L. Zhao, Z. Xu, C. Kong, and W. Gong, "The improvement of near-ultraviolet electroluminescence of ZnO nanorods/MEH-PPV heterostructure by using a ZnS buffer layer," *Organic Electronics*, vol. 12, pp. 92-97, 2011.
[64] M. Slootsky, X. Liu, V. M. Menon, and S. R. Forrest, "Room temperature Frenkel-Wannier-Mott hybridization of degenerate excitons in a strongly coupled microcavity," *Physical review letters*, vol. 112, p. 076401, 2014.
[65] T. Plehn, D. Ziemann, and V. May, "Simulations of Frenkel to Wannier–Mott Exciton Transitions in a Nanohybrid System," *The Journal of Physical Chemistry C*, vol. 122, pp. 27925-27934, 2018.
[66] Z. Wang, C. Wang, H. Zhang, Z. Liu, B. Zhao, and W. Li, "The application of charge transfer host based exciplex and thermally activated delayed fluorescence materials in organic light-emitting diodes," *Organic Electronics*, vol. 66, pp. 227-241, 2019.
[67] M. Tabachnyk, B. Ehrler, S. Gélinas, M. L. Böhm, B. J. Walker, K. P. Musselman, N. C. Greenham, R. H. Friend, and A. Rao, "Resonant energy transfer of triplet excitons from pentacene to PbSe nanocrystals," *Nature materials*, vol. 13, pp. 1033-1038, 2014.
[68] D. Ellis, J. Hill, S. Wakimoto, R. Birgeneau, D. Casa, T. Gog, and Y.-J. Kim, "Charge-transfer exciton in La 2 CuO 4 probed with resonant inelastic x-ray scattering," *Physical Review B*, vol. 77, p. 060501, 2008.
[69] K. Gautam, I. Singh, P. Bhatnagar, and K. R. Peta, "Single mode waveguiding effect of ZnO nanorods to enhance the luminance of conjugated polymer based light emitting diodes," *Journal of Luminescence*, vol. 204, pp. 59-63, 2018.
[70] W.-C. Ke, C.-Y. Chiang, W. Son, and F.-W. Lee, "InGaN-based light-emitting diodes grown on various aspect ratios of concave nanopattern sapphire substrate," *Applied Surface Science*, vol. 456, pp. 967-972, 2018.

[71] K. S. Kim, S. M. Kim, H. Jeong, M. S. Jeong, and G. Y. Jung, "Enhancement of light extraction through the wave-guiding effect of ZnO sub-microrods in InGaN blue light-emitting diodes," *Advanced Functional Materials,* vol. 20, pp. 1076-1082, 2010.
[72] C. Brunet, B. Ung, P.-A. Bélanger, Y. Messaddeq, S. LaRochelle, and L. A. Rusch, "Vector mode analysis of ring-core fibers: Design tools for spatial division multiplexing," *Journal of Lightwave Technology,* vol. 32, pp. 4046-4057, 2014.
[73] D. Gloge, "Weakly guiding fibers," *Applied optics,* vol. 10, pp. 2252-2258, 1971.
[74] C. Y. Tsao, D. N. Payne, and W. A. Gambling, "Modal characteristics of three-layered optical fiber waveguides: a modified approach," *JOSA A,* vol. 6, pp. 555-563, 1989.
[75] S. Choi, K. Oh, W. Shin, C. Park, U. Paek, K. Park, Y. C. Chung, Y. Kim, and Y. Lee, "Novel mode converter based on hollow optical fiber for gigabit LAN communication," *IEEE Photonics Technology Letters,* vol. 14, pp. 248-250, 2002.
[76] C. R. Doerr, N. Fontaine, M. Hirano, T. Sasaki, L. Buhl, and P. Winzer, "Silicon photonic integrated circuit for coupling to a ring-core multimode fiber for space-division multiplexing," in *European Conference and Exposition on Optical Communications*, 2011, p. Th. 13. A. 3.
[77] H. Huang, F. Deng, J. Xiang, S. Li, and S. Lan, "Plasmon-exciton coupling in dielectric-metal hybrid nanocavities with an embedded two-dimensional material," *Applied Surface Science,* vol. 542, p. 148660, 2021.
[78] A. Faraon, P. E. Barclay, C. Santori, K.-M. C. Fu, and R. G. Beausoleil, "Resonant enhancement of the zero-phonon emission from a colour centre in a diamond cavity," *Nature Photonics,* vol. 5, pp. 301-305, 2011.
[79] O. Franek, "Efficient calculation of near fields in the FDTD method," in *2011 International Conference on Electromagnetics in Advanced Applications*, 2011, pp. 1009-1012.
[80] X.-W. Chen and S. He, "Optical Modeling of Photoluminescence of Multilayered Semiconductor Nanostructures: Nanowires, Nanotubes and Nanocables," *Nanowires,* p. 337, 2010.
[81] H.-Y. Ryu, "Evaluation of light extraction efficiency of GaN-based nanorod light-emitting diodes by averaging over source positions and polarizations," *Crystals,* vol. 8, p. 27, 2018.
[82] H. D. Cho, D. Y. Kim, and J.-K. Lee, "ZnO Nanorod/Graphene Hybrid-Structures Formed on Cu Sheet by Self-Catalyzed Vapor-Phase Transport Synthesis," *Nanomaterials,* vol. 11, p. 450, 2021.
[83] Y. Wu, Y. Dai, S. Jiang, C. Ma, Y. Lin, D. Du, Y. Wu, H. Ding, Q. Zhang, and N. Pan, "Interfacially Al-doped ZnO nanowires: greatly enhanced near band edge emission through suppressed electron–phonon coupling and confined optical field," *Physical Chemistry Chemical Physics,* vol. 19, pp. 9537-9544, 2017.